MDPI

Article

Optimized Unilateral Magnetic Resonance Sensor with Constant Gradient and Its Applications in Composite Insulators

Pan Guo [1,*]**, Chenjie Yang** [1]**, Jiamin Wu** [2,3] **and Zheng Xu** [4]

1   College of Physics and Electronic Engineering, Chongqing Normal University, Chongqing 401331, China; 2019051107004@stu.cqnu.edu.cn
2   Shenzhen Academy of Aerospace Technology, Shenzhen 518057, China; wujiamin@chinasaat.com
3   School of Mechatronics Engineering, Harbin Institute of Technology, Harbin 150006, China
4   School of Electrical Engineering, Chongqing University, Chongqing 400044, China; xuzheng@cqu.edu.cn
*   Correspondence: guopan@cqnu.edu.cn; Tel.: +86-135-2747-2600

Abstract: In this study, an optimized unilateral magnetic resonance sensor with a three-magnet array is presented for assessing the aging of composite insulators in power grids. The sensor's optimization involved enhancing the static magnetic field strength and the homogeneity of the RF field while maintaining a constant gradient in the direction of the vertical sensor surface and maximizing homogeneity in the horizontal direction. The center layer of the target area was positioned 4 mm from the coil's upper surface, resulting in a magnetic field strength of 139.74 mT at the center point of the area, with a gradient of 2.318 T/m and a corresponding hydrogen atomic nuclear magnetic resonance frequency of 5.95 MHz. The magnetic field uniformity over a 10 mm $\times$ 10 mm range on the plane was 0.75%. The sensor measured 120 mm $\times$ 130.5 mm $\times$ 76 mm and weighed 7.5 kg. Employing the optimized sensor, magnetic resonance assessment experiments were conducted on composite insulator samples utilizing the CPMG (Carr–Purcell–Meiboom–Gill) pulse sequence. The T_2 distribution provided visualizations of the T_2 decay in insulator samples with different degrees of aging.

Keywords: aging assessment; composite insulator; transverse relaxation time (T_2); unilateral magnetic resonance (UMR)

1. Introduction

Insulators play a critical role in ensuring the safety of power systems [1]. As depicted in Figure 1, composite insulators have gained popularity in electric power systems because of their light weight, good anti-fouling and flash performance, and high mechanical strength. However, the prolonged exposure of composite insulators to electric fields, ultraviolet light, acid rain, and fouling leads to their aging and the deterioration of their electrical and mechanical properties, which potentially jeopardizes the power supply reliability of the power grid [2]. Therefore, testing the performance of composite insulators, assessing the degree of insulator aging, determining whether replacements are necessary, troubleshooting the power grid, and improving the efficiency of equipment condition maintenance are critical to ensuring the safe operation of the power system [3,4].

Unilateral magnetic resonance (UMR) sensors, comprising an open permanent magnet structure and surface radio frequency (RF) coils, offer a sensitive volume external to the sensor, facilitating the non-invasive investigation of objects of any size [5–7]. This feature enables a broad range of industrial applications, particularly when paired with a compact magnetic resonance (MR) console, creating a portable MR system.

Over the past three decades, several designs of unilateral magnets have been proposed to generate a static magnetic field B_0 [8–12]. These designs can be broadly classified into two categories based on the distribution of the static magnetic field. The first category of magnets creates a saddle point of B_0, where the derivatives of B_0 are nulled around the

saddle point. This design allows for a large excitation volume and reduces the diffusive attenuation of gradients caused by molecular motion. The second category of magnets generates a linear B0 distribution, creating a constant gradient perpendicular to the magnet surface. This type of magnet produces a well-defined sensitive volume, typically consisting of a thin layer or a set of layers. As a result, these magnets offer spatial information that can be utilized to investigate layered objects.
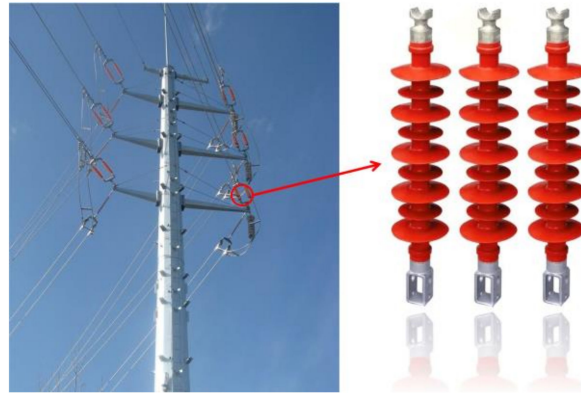

Figure 1. Composite insulators.

NMR-MOUSE (Nuclear Magnetic Resonance–Mobile Universal Surface Explorer) and its variations have been developed to establish a strong gradient (above 20 T/m) in the static magnetic field B_0 [13–15]. However, this strong gradient can cause a relatively large change in the magnetic field strength within the sensitive layer due to temperature and the presence of ferromagnetic objects. Additionally, it results in a thin sensitive layer, which can be problematic for applications that involve diffusive attenuation or motion-induced decay. To address this issue, an optimized magnet geometry for NMR-MOUSE was proposed in a recent study, reducing the gradient from 20 T/m to 1.87 T/m [16]. Another magnet design was suggested, which utilizes a shaped pole piece to create a well-controlled gradient ranging from 0.3 to 2.5 T/m [17]. The same team also presented a three-magnet array unilateral magnet design that is easy and safe to install and compact in size. The gradient of this magnet was reduced to 0.63 T/m, but the strength of B_0 was also decreased to 0.047 T [16,17]. The characteristics of these sensors described above are that there is a strong magnetic field gradient when the magnetic field intensity is high, or that the magnetic field intensity is correspondingly considerably reduced when the magnetic field gradient is reduced to a certain value.

In this study, we aimed to optimize the design of a three-magnet array unilateral magnet to balance the strength of B_0 and its constant gradient, achieving a larger sensitive volume while keeping a modest excitation bandwidth. This allows for the use of low-power RF amplifiers to enhance the mobility of the UMR system. The resulting UMR sensor (Figure 2) has dimensions of 120 mm × 130.5 mm × 76 mm and a mass of 7.5 kg. The center layer of the sensitive volume is positioned 4 mm away from the upper surface of the coil, and the magnetic field at the center point of the area is 0.139 T, with a gradient of 2.318 T/m. The corresponding hydrogen atomic nuclear magnetic resonance frequency is 5.95 MHz, and the uniformity of the magnetic field in the range of 10 mm × 10 mm on the plane is 0.75%.

The advantage of the sensor proposed in this paper is that it obtains a small magnetic field gradient while maintaining a certain magnetic field intensity and a small weight, so as to measure the sample with relatively small transverse relaxation time, as in the case of composite insulators. At the same time, in order to ensure the temperature stability of the static magnetic field of the sensor for engineering field measurement, a samarium cobalt magnet with high remanence temperature coefficient was employed. The sensor was compared with other similar sensors, as shown in Table 1. Additionally, the SNR of the

sensor was improved by increasing the uniformity of the static magnetic field, increasing the uniformity and intensity of the RF magnetic field, and decreasing the eddy current effect.
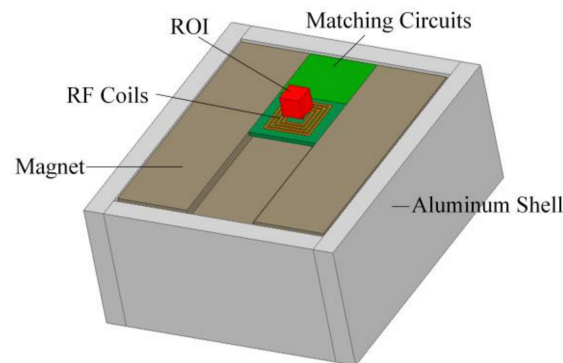

Figure 2. A schematic of the UMR sensor.

Table 1. Comparison of the sensor in this study with similar sensors.

Sensors	Frequency (MHz)	Gradient (T/m)	Dimension (cm)	Magnet Materials
NMR-MOUSE	17	20	$20 \times 20 \times 10$	$Na_2Fe_{14}B$
Mini-NMR-MOUSE	17.14	67.8	$7 \times 5 \times 7$	$Na_2Fe_{14}B$
Three-magnet array	4.26	2	$10 \times 8 \times 5$	$N_{48}NaFeB$
The sensor in this work	5.95	2.318	$12 \times 13.05 \times 7.6$	$(SmGd)_2(CoFeCuZr)_{17}$

To validate the effectiveness of the optimized unilateral NMR sensor, we conducted assessment experiments on the aging of composite insulators using a prototype of the sensor. Insulator samples with varying levels of aging were set up, and NMR assessments were conducted by analyzing the relationship between the NMR signal and the sample's aging time.

2. Materials and Methods

The sensor to be optimized is shown in Figure 3, which comprises of the magnet and the RF coil. According to Richards and Hoult [18,19], the signal-to-noise ratio (SNR) of NMR measurements can be expressed as:

$$SNR = \frac{N\gamma^3\hbar^2 I(I+1)}{6\sqrt{2}(\kappa_B T)^{\frac{3}{2}}} \cdot B_0^2 \cdot \frac{V_{sample}}{\sqrt{\Delta f}} \cdot \frac{B_1/i}{\sqrt{R}} \tag{1}$$
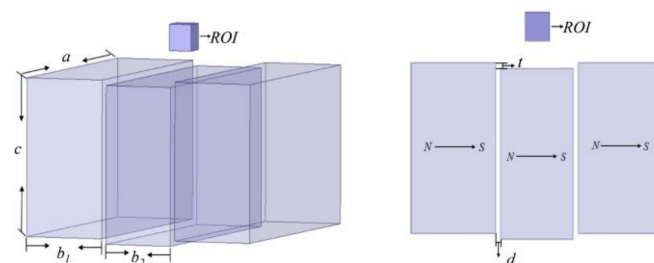

Figure 3. Schematic diagram of three-magnet array structure.

To improve the SNR, under the condition that the tested sample and the experimental environment are determined, V_{sample}, B_0^2, B_1/i should be maximized, and at the same time, $\triangle f$, $\sqrt{R}$ minimized, where B_0 is the static magnetic field generated by the magnet and B_1/i is the magnetic field generated by the RF coil when the unit current passes through.

V_{sample} is defined by the homogeneity of B_0 and B_1, which is usually called the ROI (region of interest), and $\triangle f$ and $\sqrt{R}$ are the bandwidth resistance of the RF coil. The magnet and RF coil optimization will be discussed as follows, respectively.

2.1. Magnet Optimization

Magnet optimization was carried out by calculating its magnetic field distribution. The remanent magnetization of a permanent magnet is equivalent to a toroidal current around the surface of the permanent magnet block, for which the magnetic field distribution of the permanent magnet can be calculated using the Biot–Savard law [20,21]. The magnetic field strengths B_x, B_y, and B_z generated at any point P (x, y, z) in space can be expressed by Equations (2)–(6), where dB_x, dB_y, and dB_z are the magnetic inductance components in the x, y, and z directions at point P.

$$B_x = \int_0^h dB_x = -\frac{K}{2}\left[\begin{array}{c} \Gamma(a-x,y,z) + \Gamma(a-x,b-y,z) \\ -\Gamma(x,y,z) - \Gamma(x,b-y,z) \end{array}\right]\Big|_0^h \tag{2}$$

$$B_y = \int_0^h dB_y = -\frac{K}{2}\left[\begin{array}{c} \Gamma(b-y,x,z) + \Gamma(b-y,a-x,z) \\ -\Gamma(y,x,z) - \Gamma(y,a-x,z) \end{array}\right]\Big|_0^h \tag{3}$$

$$\begin{aligned} B_z = \int_0^h dB_z = -K[&\phi(y,a-x,z) + \phi(b-y,a-x,z) \\ &+\phi(x,b-y,z) + \phi(a-x,b-y,z) + \phi(b-y,x,z) \\ &+\phi(y,x,z) + \phi(a-x,y,z) + \phi(x,y,z)]\Big|_0^h \end{aligned} \tag{4}$$

$$\Gamma(\gamma_1, \gamma_2, \gamma_3) = \ln \frac{\sqrt{\gamma_1{}^2 + \gamma_2{}^2 + (\gamma_3 - z_0)^2} - \gamma_2}{\sqrt{\gamma_1{}^2 + \gamma_2{}^2 + (\gamma_3 - z_0)^2} + \gamma_2} \tag{5}$$

$$\phi(\phi_1, \phi_2, \phi_3) = \left\{ \begin{array}{l} \arctan\left[\dfrac{\phi_1}{\phi_2}\dfrac{\phi_3 - z_0}{\sqrt{\phi_1{}^2 + \phi_2{}^2 + (\phi_3 - z_0)^2}}\right] \\ 0 \end{array}\right. \tag{6}$$

where $K = \mu_0 J/4\pi$ is the magnetic permeability in a vacuum and J is the surface current density. Γ is the notation of the functions of the independent variables γ_1, γ_2, and γ_3. ϕ is a functional of the independent variables $\phi1$, $\phi2$, and $\phi3$. $[\cdot]|_0^h$ denotes the subtraction of the function $[\cdot]$ between the values at $z = h$ and $z = 0$. Therefore, the field strength at point P is:

$$B = \sqrt{B_x{}^2 + B_y{}^2 + B_z{}^2} \tag{7}$$

Figure 4a illustrates that the structure of the three-magnet combination is determined by the spacing d between the central magnet (with dimensions a = 120 mm, b = 30 mm, c = 60 mm) and the external magnet (with dimensions a = 120 mm, b = 35 mm, c = 60 mm), as well as the drop height h. For this study, the relative positions of the central and external magnets were adjusted to obtain a static magnetic field with a constant gradient in the target area. The spacing d was fixed at 2 mm, while the effect of the drop height h on the uniformity of the magnetic field in the target area was investigated. To simulate the magnet structure with different drop heights, the center of the upper surface of the magnet combination was used as the coordinate origin and located on the same plane as the upper surface of the external magnet. The magnetic induction intensity corresponding to different h values, distributed along the Z-axis, is shown in Figure 4b.
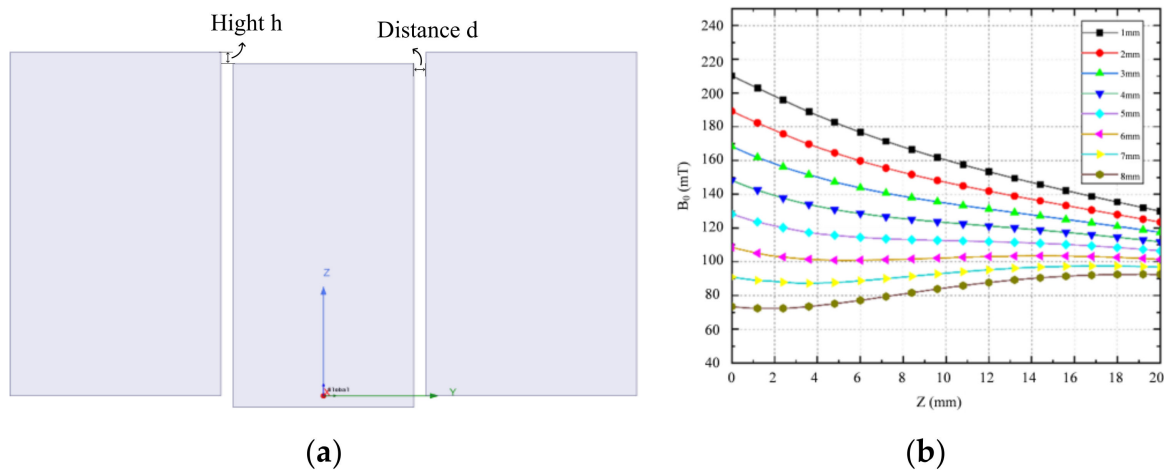
Figure 4. (**a**) Schematic diagram of the combined magnet, and (**b**) its magnetic field distribution along the *Z*-axis with h.

Based on the results shown in Figure 4b, it can be concluded that for drop heights of 1 mm, 2 mm, and 3 mm, the curve decreases linearly and maintains a constant magnetic field gradient within the target area. Additionally, to ensure a constant magnetic field gradient, it is important to also achieve a uniform magnetic field within the target plane (located at z = 13 mm). To simplify the process of optimizing the magnet, the magnetic field uniformity across the entire target plane is expressed as the uniformity of the two midlines (defined as xline and yline) along the X- and *Y*-axis directions.

$$P = \frac{(B_i - B_{centre}) \times 100}{B_{centre}} \tag{8}$$

where B_i is the magnetic field strength at each point on the midline, and B_{centre} is the magnetic field strength at the center of the target surface.

The simulation results presented in Figure 5 show the changes in the magnetic field uniformity of the two central lines as a function of the drop height (h) of the three-magnet structure. As h decreases from 3 mm to 1 mm, the Yline uniformity changes from an upper concave to a lower concave shape, indicating the existence of an optimal value of h between 1 mm and 2 mm for achieving optimal magnetic field uniformity on the Yline. While the size of h also affects the magnetic field uniformity on the Xline, its effect is not significant. Based on several simulations, we determined that the optimal magnetic field uniformity on the target surface is achieved when h = 2 mm. Although the uniformity on the Xline is not as good as on the Yline, the effect is still significant compared to other h values.

After analyzing the simulations of the magnet structure with different drop heights, a drop height of 2 mm was chosen between the central magnet and the external magnet to optimize the uniformity of the magnetic field. To verify the uniformity, the magnetic field distribution was simulated in each of the three planes of the target area. The magnetic field distribution at the center level is shown in Figure 6a, which reveals a magnetic field intensity of 139.74 mT at the center point with a deviation of 0.48 mT, resulting in a uniformity of 0.34% for this plane. Figure 6b,c present the magnetic field distribution at two perpendicular planes in the target area, showing that the contours are almost parallel, indicating that the magnetic field gradient along the Z-axis is a constant value. The magnetic field strength decreases from 153 mT to 128 mT in the target area, with a longitudinal gradient of 2.5 T/m, as shown in Figure 7.
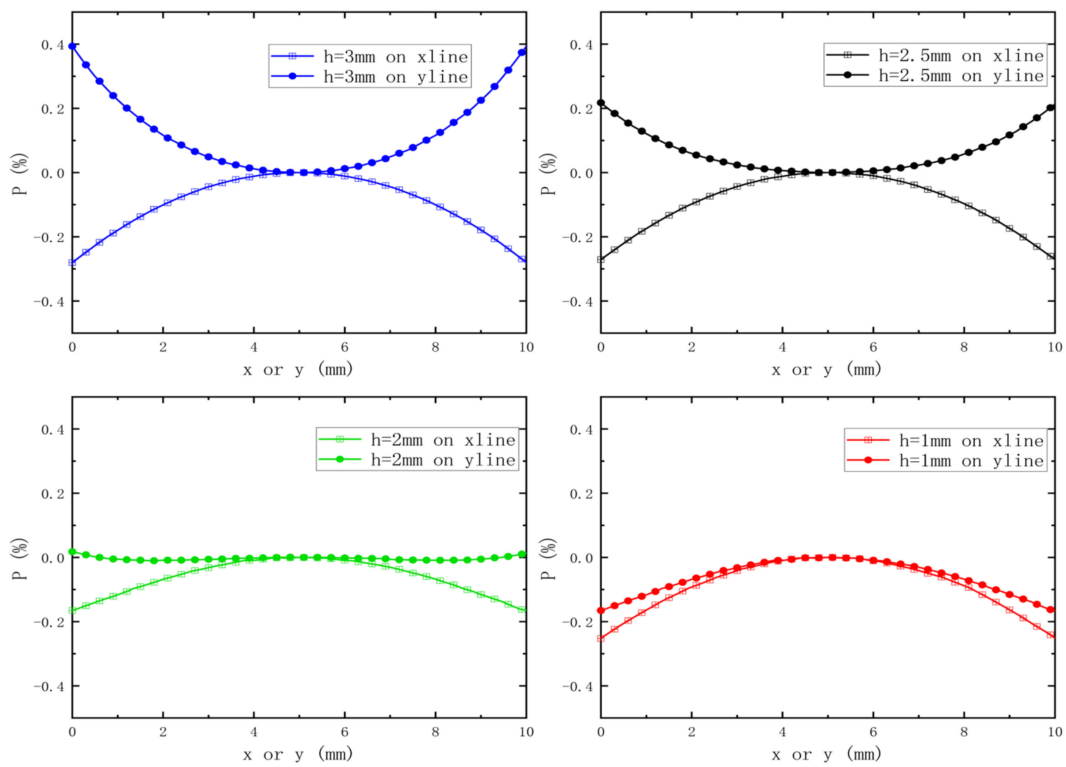
Figure 5. The variation law of the uniformity of the magnetic field of the two medians with a change in h.
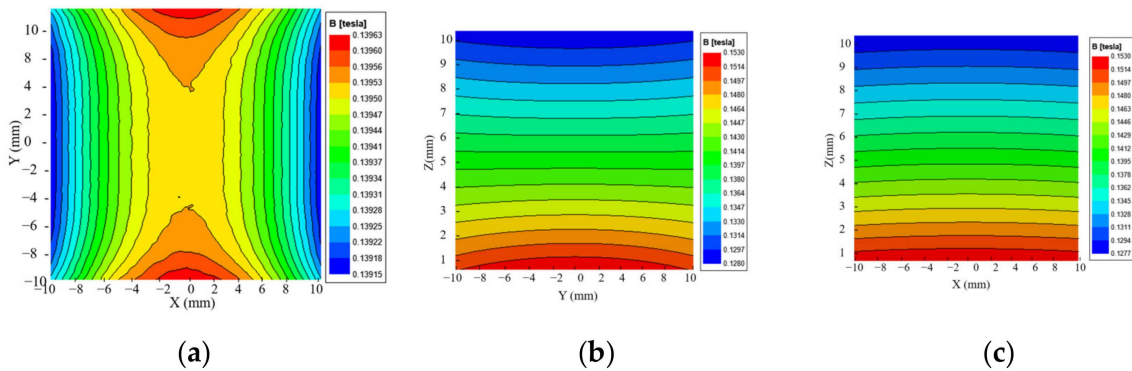

(**a**)   (**b**)   (**c**)

Figure 6. Magnetic field distribution in each plane at h = 2 mm. (**a**) XOY plane. (**b**) YOZ plane. (**c**) XOZ plane.
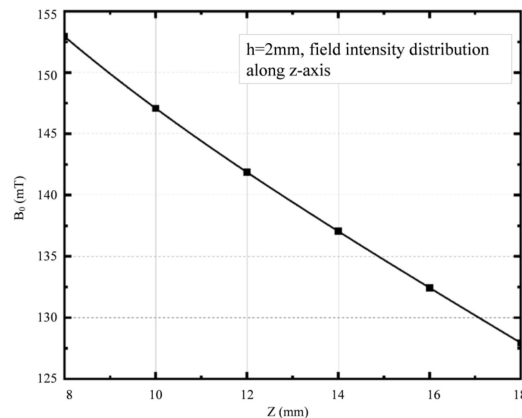

Figure 7. Magnetic field intensity distribution along Z-axis at h = 2 mm.

2.2. RF Coil Optimization

When designing an RF coil to be used in conjunction with the current magnet, three practical considerations must be taken into account [22–24]. First, the coil must generate a sensitivity spot of 10 mm × 10 mm at z = 6 mm, where the magnet provides a homogeneous magnetic field on the XOY plane. Second, to prevent eddy current effects caused by close contact with the magnet, the wiring area of the RF coil must be restricted to 25 mm × 25 mm. Third, the coil inductance should be kept to a minimum to avoid possible detuning due to load changes introduced during the experiment. Therefore, the optimization objectives to obtain the optimal RF coil structure were chosen as B_1 field intensity, excitation depth, and B_1 uniformity on the XOY plane.

To optimize the RF coil, FEM simulation using commercial software such as Ansys Maxwell (ANSYS, Inc., Canonsburg, PA, USA) was employed. Based on the magnet optimization result, the nuclear magnetic resonance frequency is 5.95 MHz, which means that the wavelength of the electromagnetic wave emitted or received by the coil is 51.7 m. Due to the limited wiring area, the length of the coil winding is much less than the wavelength, and hence, the phase difference between the RF magnetic field generated by the RF coil passeing through AC and DC is negligible. To simplify the calculation, DC was used instead of AC to compute the B_1 distribution in the simulation.

The simulation was carried out using the finite element method, with the current passing through the coil set to 1 A and the wire width and spacing both set to 1 mm. The number of turns in the coil was varied in the simulation, with values of 3, 4, 5, and 6 tested. The B_1-related parameters generated by different coil turns are shown in Table 2. The uniformity of the B_1 field in the target XOY plane was defined as follows:

$$U = 2\frac{B_{1\text{max}} - B_{1\text{min}}}{B_{1\text{max}} + B_{1\text{min}}} \times 100\% \tag{9}$$

Table 2. B_1 related parameters generated by different coil turns.

Turns	$B_{1\text{max}}$ (μT)	$B_{1\text{min}}$ (μT)	U
3	111	109	99.05%
4	151	134	94.04%
5	184	144	87.80%
6	191	143	85.63%

After considering the uniformity and strength of the B_1 field, it was found that when the number of turns in the coil was set to 4, both the uniformity and strength were satisfactory. However, to generate a stronger magnetic field, the coil structure can be further modified. For instance, increasing the intensity of B_1 can be achieved by transforming the single-layered coil into a double-layered coil, with each layer containing 4 turns. To minimize the distributed capacitance that may arise from the two parallel live wires, the wires of the second layer should be arranged alternately with the wires of the first layer, as depicted in Figure 8.
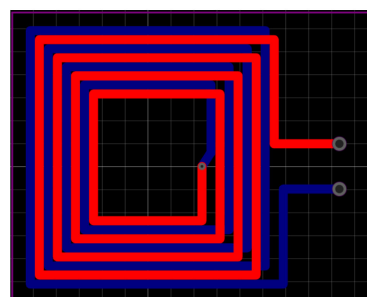

Figure 8. The two-layer coil wiring structure.

The RF coils were fabricated on a PCB substrate, which is typically available in standard thicknesses of 0.2 mm, 0.4 mm, 0.8 mm, 1 mm, 1.6 mm, and 2 mm. To evaluate the effect of PCB thickness on the B_1 field, simulations were conducted, and the results are presented in Table 3. As shown, the uniformity and intensity of the B_1 field decrease with increasing PCB thickness.

Table 3. B_1 related parameters generated by different thicknesses of PCB.

Thickness (mm)	B_{1max} (μT)	B_{1min} (μT)	U
0.2	322	289	94.50%
0.4	318	284	94.30%
0.8	313	278	94.08%
1.6	309	274	93.94%

After considering various factors, such as B_1 intensity and uniformity, excitation depth, and manufacturing difficulty, a double-layer coil with 4 turns and a 0.4 mm PCB thickness was chosen. The B_1 field distribution for this coil configuration is shown in Figure 9. Finally, the optimal coil, which was made of copper with a thickness of 2 OZ, had two layers with four turns that were 1 mm wide. The distance between two leads was 1 mm, and that between the two layers was 0.4 mm.
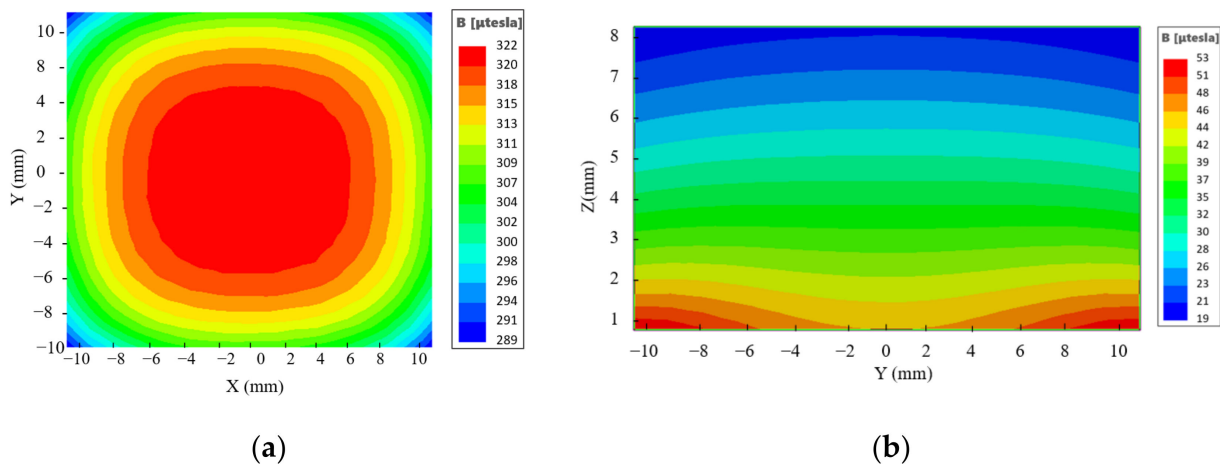

(a)　　　　　　　　　　　　　　　　　　　　　　　　　　**(b)**

Figure 9. B_1 distribution of the optimal RF coil. (**a**) XOY plane. (**b**) YOZ plane.

2.3. Eddy Current Effect Optimization

In order to optimize the coupling between the magnet and RF coil and minimize the impact of eddy currents on the B_1 field strength, a 1 mm thick copper layer was used to shield the magnet. To investigate the effect of the RF coil and magnet on the B_1 magnetic field and determine the different distances (D) between them, finite element simulations were conducted using a 30 mm $\times$ 30 mm $\times$ 10 mm copper cube instead of the magnet for simplicity. The D values chosen were 3, 5, 7, and 10 mm. Additionally, the B_1 field when the RF coil operates independently was also included in the optimization process for comparison, to better evaluate the optimization results. Figure 10a presents a schematic diagram of the RF coil and magnet locations in the simulation.

The B_1 profiles were measured for each D value, and the results are depicted in Figure 10b. The measurements revealed that the magnetic field intensity in the target region is highest when the RF coil is working alone, while the B_1 field strength decreases with decreasing D values. At a depth of 4 mm, when D was set to 3 mm, only 24% of B_1 was retained. However, when D was increased to 10 mm, B_1 reached 95%, and the impact of the eddy current effect on the reduction in B_1 became negligible. Thus, a value of D = 10 mm was selected as the final distance between the RF coil and the magnet.
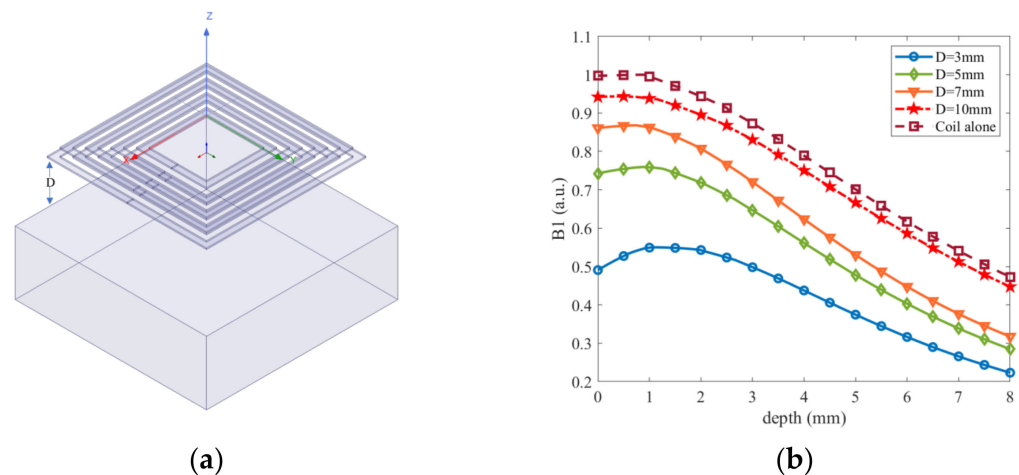
Figure 10. (**a**) Schematic diagram of the location of the RF coil and magnet, (**b**) Distribution curves of RF magnetic field along the Z-axis.

3. Results and Discussion

3.1. Field Measurements

Fro magnets of the sizes given above, to improve the temperature stability of the magnetic field of the magnet, we employed $(SmGd)_2(CoFeCuZr)_{17}$ (YXG32, Ning-gang Permanent Magnetic Materials Co., Ltd., Ningbo, China) as the permanent magnet material since it has a low temperature coefficient ($-0.035\%/°C$) and high remanence (Br 1.10–1.13 Tesla) between 20 °Cand 150 °C. The performance parameters of samarium cobalt permanent magnets are shown in Table 4.

Table 4. Performance parameters of samarium cobalt permanent magnets.

Model	Remanence	Coercivity	Intrinsic Coercivity	Maximum Magnetic Energy Product	Temperature Coefficient of Remanence
	$B_r(\mathbf{T})$	$H_{cb}(\mathbf{KA/m})$	$H_{cj}(\mathbf{KA/m})$	$(BH_{cb})_{max}(\mathbf{KA/m})$	$(\%/°\mathbf{C})$
XYG-32	1.10–1.13	812–860	≥ 1433	230–255	-0.035

The BELL8030 Gauss meter (F.W. Bell Inc., Portland, OR, USA) and a computer-controlled 3-axis positioning system were utilized to measure the magnetic field of the optimized sensor prototype. The three-dimensional coordinates of the measurement points are depicted in Figure 11a, with the center of the upper surface of the RF coil serving as the origin of the coordinates, and the plane where the upper surface is located at z = 0 mm. A profile of the magnetic field distribution in the target area is illustrated in Figure 11b. Additionally, Figure 12 depicts the magnetic field distribution on three planes in the target area.

The center level of the target area was found to be 4 mm away from the upper surface of the coil, with a magnetic field at the center point of the area of 139.74 mT and a gradient of 2.318 T/m. This corresponds to the nuclear magnetic resonance frequency of hydrogen atoms of 5.95 MHz. Additionally, the magnetic field uniformity in the range of 10 mm × 10 mm on this level was calculated to be 0.75%.

(a)   (b)

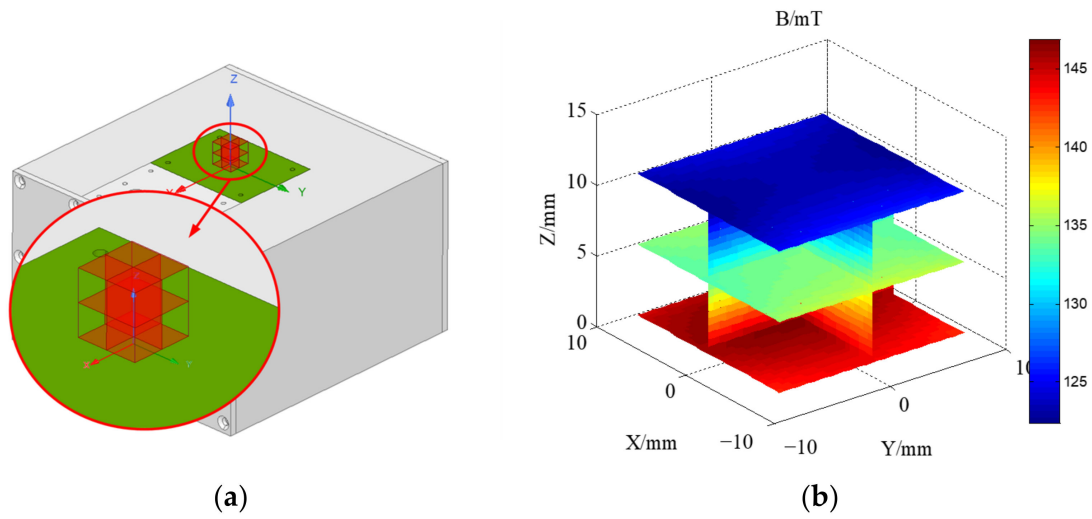**Figure 11.** (**a**) Schematic diagram of the magnetic field test surface of the magnet. (**b**) Magnetic field distribution on the test surface.

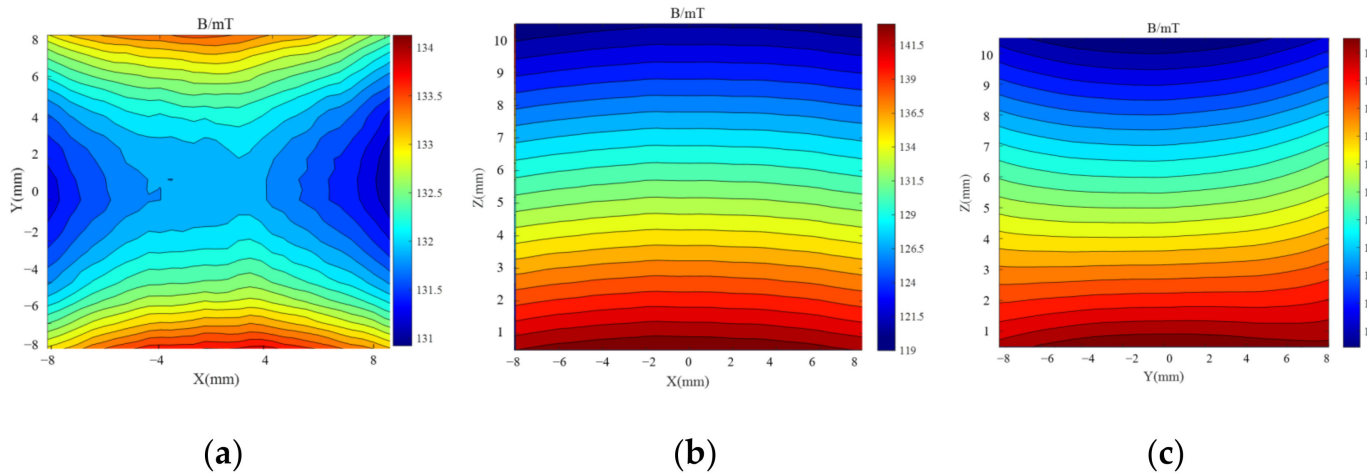(a)   (b)   (c)

Figure 12. The B0 distribution. (**a**) Measuring plane z = 5 mm. (**b**) Measurement plane y = 0 mm. (**c**) Measuring plane x = 0 mm.

3.2. Sensitivity Map

The area of the sensitive region of a unilateral NMR sensor is determined by the static magnetic field B_0 and the RF field B_1 with a complex functional relationship [25,26]. The calculation process will be briefly described below. The electric potential $\xi(t)$ induced in the coil can be written as:

$$\xi(t) = \int \Phi(r)(\gamma B_0(r))\left(\frac{\chi}{\mu_0}B_0(r)\right)\frac{B_1(r)}{I}F(\Delta\omega(r))m_{xy}(r,t)dr \tag{10}$$

where Φ denotes the local spin density in the sample, γ is the spin ratio, χ is the nuclear magnetization, and $\chi = 4.04 \times 10^{-9}$ in MKS; the first B0 term is the induction detection value based on Faraday's law assumptions when measuring the NMR signal, and the second B0 term denotes the thermal longitudinal magnetization intensity $M_0(r)$; $B_1(r)/I$ denotes the magnetization efficiency of the receiver coil at point r; $F(\Delta\omega_0(r))$ is the frequency response of the detection system, including the response of the tuned receiver coil and any hardware and or software filters; and $m_{xy}(r,t)$ denotes the transverse magnetization at point r and time t, normalized to $M_0(r)$. Thus, the main task of calculating the sensitivity region is to find $m_{xy}(r,t)$ a given pulse sequence in a static magnetic field.

Assuming that $|B_0(r)| \gg |B_1(r,t)|$ neglects the effects of relaxation and diffusion, the asymptotic CPMG signal can be described as in Equation (1).

$$m_{axy}(\Delta\omega_0, \omega_1) = \frac{\omega_1}{\Omega} \times \frac{\sin(\Omega t_{90})}{1 + \left[\frac{\Omega}{\omega_1}\sin(\frac{\Delta\omega_0 \cdot t_E}{2})\cot(\frac{\Omega \cdot t_{180}}{2}) + \frac{\Delta\omega_0}{\omega_1}\cos(\frac{\Delta\omega_0 \cdot t_E}{2})\right]^2} \qquad (11)$$

where $\Omega = \sqrt{\omega_1^2 + \Delta\omega_0^2}$ is the chapter frequency of the spin during the RF pulse, and $\Delta\omega_0 = \omega_{RF} - \gamma|B_0|$ and $\omega_1 = \gamma|B_{1c}|$ are scalars, where B_{1c} is the component of the RF field B_1 and this component is orthogonal to the main magnetic field B_0.

$$B_{1c} = \frac{1}{2}\left[B_1(r) - B_0(r)\frac{(B_1(r)\cdot B_0(r))}{(B_0(r)\cdot B_0(r))}\right] \qquad (12)$$

To generate a sensitivity map for the unilateral NMR sensor, several steps were taken. First, vector maps of the main magnetic field B_0 and the RF field B_1 at the central level were obtained. Then, the value of B_{1c} was calculated for each point in the region using Equation (12). Next, the maximum value of B_{1c} (maxy) was calculated using Equation (11). Finally, maxy was substituted into Equation (10) to obtain the signal voltage, which was calculated using MATLAB software to generate the unilateral NMR sensitivity maps. The resulting maps are shown in Figure 13.
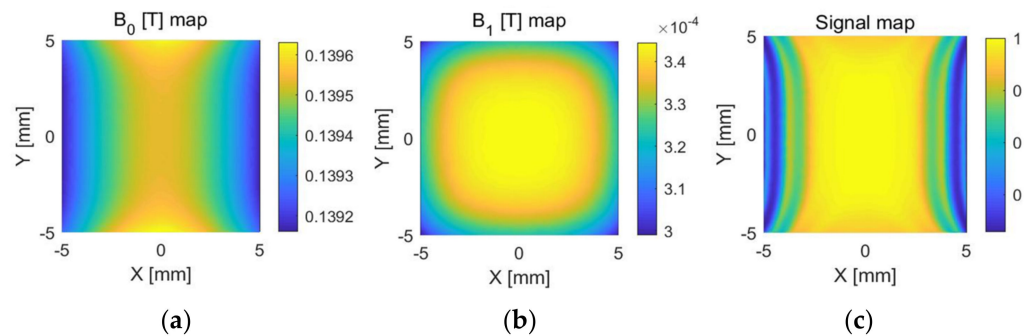

Figure 13. (**a**) Magnetic field distribution of B0. (**b**) Magnetic field distribution of B_1. (**c**) Projection of the NMR sensitivity map onto the z = 4 mm plane.

3.3. Aging Assessment of Composite Insulators

To evaluate the sensor's capabilities, an experiment was conducted to assess the aging of composite insulators. The samples were aged inside a UV-accelerated aging chamber for 0 h, 24 h, and 48 h. These samples were placed in the central region of the RF coil of the unilateral NMR sensor, as depicted in Figure 14. The transverse relaxation time T2 of the aged insulators was measured using the Carr–Purcell–Meiboom–Gill (CPMG) sequence.

Figure 14. Assessment of aged insulator samples.

The experimental parameters were carefully selected and set. The resonant frequency used was f = 5.95 MHz, with the $(\pi)/2$ and π pulse attenuations set to −20 dB and −14 dB, respectively. Each point was sampled for 0.5 µs, with an echo time of 150 µs and a pulse length of 5 µs. The experiment utilized 32 sampling points and scanning was performed 30 times. The CPMG echo signal obtained from the experiment was fitted using a biexponential decay curve (Figure 15), from which two T2 values were obtained.
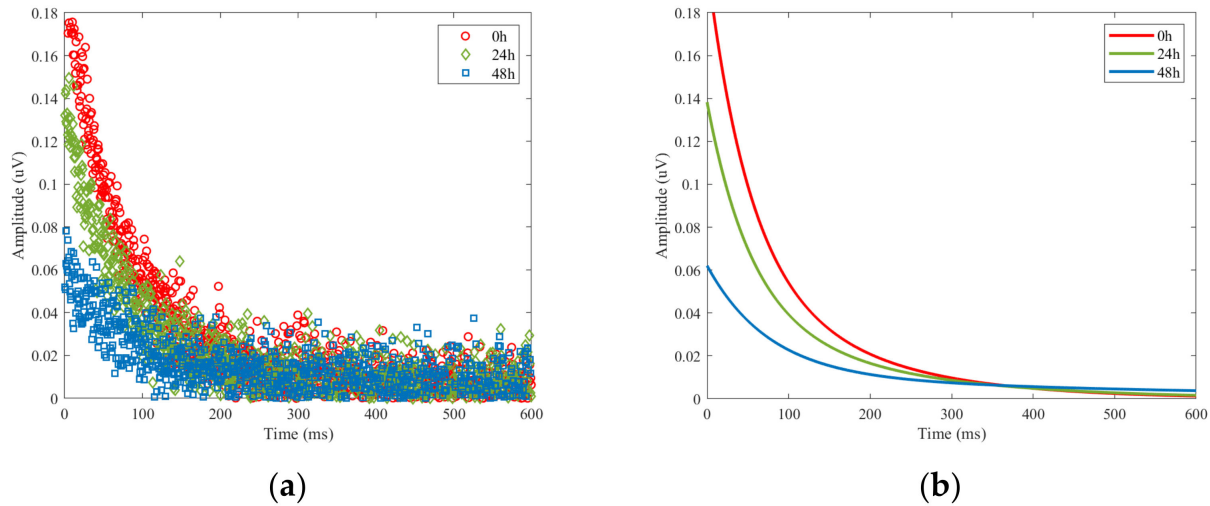

Figure 15. CPMG decay curve. (**a**) Data measured by the prototype. (**b**) The fitting curve of data in (**a**).

Figure 16 shows the T_2 trend obtained from assessments on insulators at different aging times. It can be seen that the amplitude of T_2 decreases as the aging time of the insulator increases.
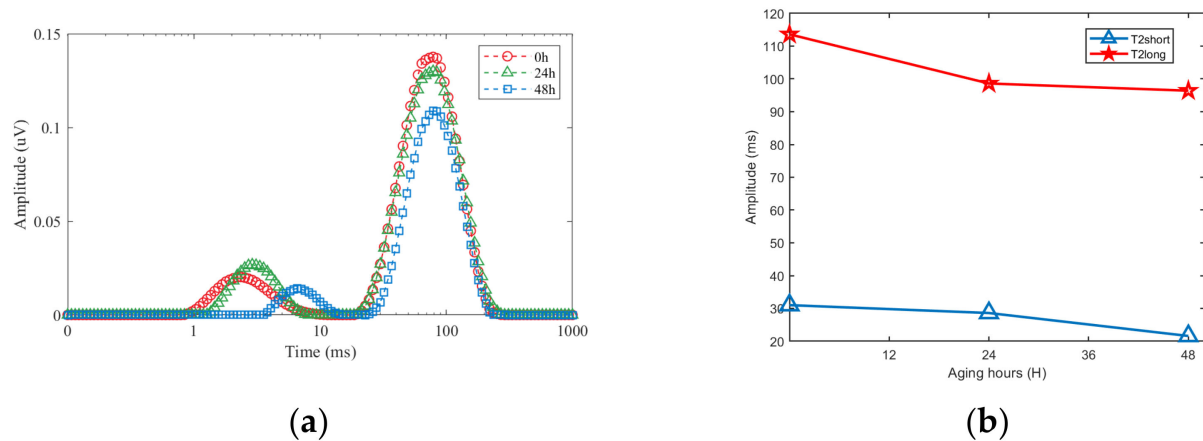
Figure 16. Analysis of NMR signal. (**a**) T_2 distribution spectrum. (**b**) Insulator aging time and its corresponding T_2.

4. Conclusions

An optimized three-magnet array sensor is proposed for the aging assessment of composite insulators. The optimization process involves increasing the static magnetic field strength and the uniformity of the RF field, while also investigating and optimizing the effect of the eddy current between the RF coil and the magnet in the B_1 field. The effectiveness of the optimized sensor is demonstrated through assessment experiments of aged insulators, where the transverse relaxation time T_2 can be effectively analyzed for insulator samples with different aging levels using CPMG pulse sequences. The obtained

transverse relaxation decay curves provide a fast and efficient method for assessing the aging levels of composite insulator samples.

References

1. Mavrikakis, N.C.; Mikropoulos, P.N.; Siderakis, K. Evaluation of Field-ageing Effects on Insulating Materials of Composite Suspension Insulators. *IEEE Trans. Dielectr. Electr. Insul.* **2017**, *24*, 490–498. [CrossRef]
2. Jiang, H.; Li, B.; Zhao, B.; Sun, Q.; Gao, C.; Chen, L. Evaluation of aging process of silicone rubber composite insulators with photothermal radiometry. *J. Phys. D Appl. Phys.* **2018**, *51*, 425304. [CrossRef]
3. Vosloo, W.; Davey, R. Power utility perspective on natural ageing and pollution performance of outdoor insulators. *IEEE Electr. Insul. Mag.* **2020**, *36*, 56–66. [CrossRef]
4. He, W.; Zhang, F.; Zhang, F.; He, Q. Effect of CeO2 on UV aging of composite insulators prepared by template-spraying method. *J. Appl. Polym. Sci.* **2022**, *140*, e53274.
5. Blümich, B.; Casanova, F.; Perlo, J.; Anferova, S.; Anferov, V.; Kremer, K.; Goga, N.; Kupferschläger, K.; Adams, M. Advances of unilateral mobile NMR in nondestructive materials testing. *Magn. Reson. Imaging* **2005**, *23*, 197–201. [CrossRef]
6. Marble, A.E.; Mastikhin, I.V.; Colpitts, B.G.; Balcom, B.J. An analytical methodology for magnetic field control in unilateral NMR. *J. Magn. Reson.* **2005**, *174*, 78–87. [CrossRef] [PubMed]
7. Proietti, N.; Capitani, D.; Lamanna, R.; Presciutti, F.; Rossi, E.; Segre, A. Fresco paintings studied by unilateral NMR. *J. Magn. Reson.* **2005**, *177*, 111–117. [CrossRef] [PubMed]
8. Proietti, N.; Capitani, D.; Pedemonte, E.; Blümich, B.; Segre, A. Monitoring degradation in paper: Non-invasive analysis by unilateral NMR. Part II. *J. Magn. Reson.* **2004**, *170*, 113–120. [CrossRef]
9. Manz, B.; Coy, A.; Dykstra, R.; Eccles, C.; Hunter, M.; Parkinson, B.; Callaghan, P. A mobile one-sided NMR sensor with a homogeneous magnetic field: The NMR-MOLE. *J. Magn. Reson.* **2006**, *183*, 25–31. [CrossRef] [PubMed]
10. Liberman, A.; Bergman, E.; Sarda, Y.; Nevo, U. Faster imaging with a portable unilateral NMR device. *J. Magn. Reson.* **2013**, *231*, 72–78. [CrossRef]
11. Kehlet, C.; Catalano, A.; Dittmer, J. Degradation of natural rubber in works of art studied by unilateral NMR and high field NMR spectroscopy. *Polym. Degrad. Stab.* **2014**, *107*, 270–276. [CrossRef]
12. Xu, Z.; Morris, R.H.; Bencsik, M.; Newton, M.I. Detection of Virgin Olive Oil Adulteration Using Low Field Unilateral NMR. *Sensors* **2014**, *14*, 2028–2035. [CrossRef]
13. Blümich, B.; Blümler, P.; Eidmann, G.; Guthausen, A.; Haken, R.; Schmitz, U.; Saito, K.; Zimmer, G. The NMR-mouse: Construction, excitation, and applications. *Magn. Reson. Imaging* **1998**, *16*, 479–484. [CrossRef]
14. Balibanu, Hailu, Eymael, Demco, and Blumich, Nuclear magnetic resonance in inhomogeneous magnetic fields. *J. Magn. Reson.* **2000**, *145*, 246–258. [CrossRef] [PubMed]
15. Perlo, J.; Casanova, F.; Blümich, B. Profiles with microscopic resolution by single-sided NMR. *J. Magn. Reson.* **2005**, *176*, 64–70. [CrossRef] [PubMed]
16. Oligschläger, D.; Glöggler, S.; Watzlaw, J.; Brendel, K.; Jaschtschuk, D.; Colell, J.; Zia, W.; Vossel, M.; Schnakenberg, U.; Blümich, B. A Miniaturized NMR-MOUSE with a High Magnetic Field Gradient (Mini-MOUSE). *Appl. Magn. Reson.* **2014**, *46*, 181–202. [CrossRef]
17. García-Naranjo, J.C.; Mastikhin, I.V.; Colpitts, B.G.; Balcom, B.J. A unilateral magnet with an extended constant magnetic field gradient. *J. Magn. Reson.* **2010**, *207*, 337–344. [CrossRef]
18. Morin, D.M.; Yan, P.; Augustine, M.P.; Balcom, B.J. An Optimized 2 MHz Unilateral Magnet with a Large Homogeneous Sensitive Spot. *Appl. Magn. Reson.* **2022**, *53*, 401–415. [CrossRef]

19. Perlo, J.; Danieli, E.; Perlo, J.; Blümich, B.; Casanova, F. Optimized slim-line logging NMR tool to measure soil moisture in situ. *J. Magn. Reson.* **2013**, *233*, 74–79. [CrossRef]
20. Shen, S.; Guo, P.; Wu, J.; Ding, Y.; Chen, F.; Meng, F.; Xu, Z. Optimized inside-out magnetic resonance probe for soil moisture measuring in situ. *J. Magn. Reson.* **2019**, *307*, 106565. [CrossRef]
21. Nakashima, Y.; Sawatsubashi, T.; Fujii, S. Nondestructive quantification of moisture in powdered low-rank coal by a unilateral nuclear magnetic resonance scanner. *Int. J. Coal Prep. Util.* **2020**, *42*, 1421–1434. [CrossRef]
22. Cooley, C.Z.; Stockmann, J.P.; Witzel, T.; LaPierre, C.; Mareyam, A.; Jia, F.; Zaitsev, M.; Wenhui, Y.; Zheng, W.; Stang, P.; et al. Design and implementation of a low-cost, tabletop MRI scanner for education and research prototyping. *J. Magn. Reson.* **2020**, *310*, 106625. [CrossRef] [PubMed]
23. Ross, M.M.B.; Wilbur, G.R.; Barrita, P.F.J.C.; Balcom, B.J. A portable, submersible, MR sensor—The Proteus magnet. *J. Magn. Reson.* **2021**, *326*, 106964. [CrossRef]
24. He, Z.; He, W. Calculating Temperature Distribution of Uniplanar Gradient Coils for Unilateral NMR Magnet Based on Fourier Analysis. *Appl. Magn. Reson.* **2016**, *47*, 613–626. [CrossRef]
25. Utsuzawa, S.; Tang, Y.; Song, Y.-Q. Inside-out NMR with two concentric ring magnets. *J. Magn. Reson.* **2021**, *333*, 107082. [CrossRef] [PubMed]
26. Xu, X.; Guo, P.; Lu, M.; Zhao, S.; Xu, Z. Optimized Portable Unilateral Magnetic Resonance Sensor for Assessing the Aging Status of Silicon Rubber Insulators. *IEEE Trans. Instrum. Meas.* **2020**, *70*, 1–11. [CrossRef]